Influence of stop and gate voltage on resistive switching of 1T1R HfO$_2$-based memristors, a modeling and variability analysis

David Maldonado [a,*], Antonio Cantudo [b], Keerthi Dorai Swamy Reddy [a], Stefan Pechmann [c], Max Uhlmann [a], Christian Wenger [a,d], Juan Bautista Roldan [b,**], Eduardo Perez [a,d]

[a] *IHP GmbH - Leibniz-Institut für innovative Mikroelektronik, 15236, Frankfurt (Oder), Germany*
[b] *Departamento de Electrónica y Tecnología de Computadores, Universidad de Granada, Facultad de Ciencias, 18071, Granada, Spain*
[c] *Chair of Micro- and Nanosystems Technology, Technical University of Munich, Munich, Germany*
[d] *Brandenburgische Technische Universität (BTU) Cottbus-Senftenberg, 03046, Cottbus, Germany*

ARTICLE INFO

ABSTRACT

Memristive devices, particularly resistive random access memory (RRAM) cells based on hafnium oxide (HfO₂) dielectrics, exhibit promising characteristics for a wide range of applications. In spite of their potential, issues related to intrinsic variability and the need for precise simulation tools and modeling methods remain a medium-term hurdle. This study addresses these challenges by investigating the resistive switching (RS) behavior of different 1T1R HfO₂-based memristive devices under various experimental conditions. Through a comprehensive experimental analysis, we extract RS parameters using different numerical techniques to understand the cycle-to-cycle (C2C) and device-to-device (D2D) variability. Additionally, we employ advanced simulation methodologies, including circuit breaker-based 3D simulation, to shed light on our experimental findings and provide a theoretical framework to disentangle the switching phenomena. Our results offer valuable insights into the RS mechanisms and variability, contributing to the improvement of robust parameter extraction methods, which are essential for the industrial application of memristive devices.

1. Introduction

Memristive devices are electronic devices with great potential in different applications such as non-volatile memory circuits, hardware cryptography, radio-frequency switches and neuromorphic computing [1–7]. Among memristive devices, phase change memory (PCM), spin-transfer torque magnetoresistive random access memory (STT-MRAM), and RRAM are prominent technologies, with RRAM cells being one of the most representative. Their structure is based on the Metal-Insulator-Metal (MIM) stack, where resistive states are dynamically modifiable through the application of voltage stimuli [8–11]. RRAMs employing HfO$_2$ dielectrics exhibit noteworthy attributes, including CMOS compatibility, rapid read/write operations, prolonged data retention, high-density integration, low-power consumption and exceptional endurance [7]. In addition, large scale RRAM crossbar arrays with a high integration density have been fabricated [7]. However, there is a wide improvement margin towards massive industrial use of these devices. In this respect, key issues to address include reducing

intrinsic variability and the lack of precise simulation tools and modeling methods, the latter connected with accurate parameter extraction techniques.

The stochastic nature of RS operations leads to cycle-to-cycle (C2C) and device-to-device (D2D) variability in memristive device performance [12–16]. Addressing both forms of variability is imperative for a thorough characterization of this technology at the production level. To achieve this, the employment of robust parameter extraction methods capable of discerning suitable programming parameters from thousands of experimental I–V characteristics simultaneously becomes fundamental.

In this work, we undertook a multifaceted approach aimed at gaining a comprehensive understanding of the physics behind the operation of the devices we have fabricated and measured. We have obtained I–V curves under ramped voltage stress (RVS). Then, we extracted RS parameters by using different numerical techniques that helped us to shed light on RS features, and mostly variability [15,17,18]. In addition, we deepened on RS operation by analyzing the role of V$_{stop}$ (for the reset
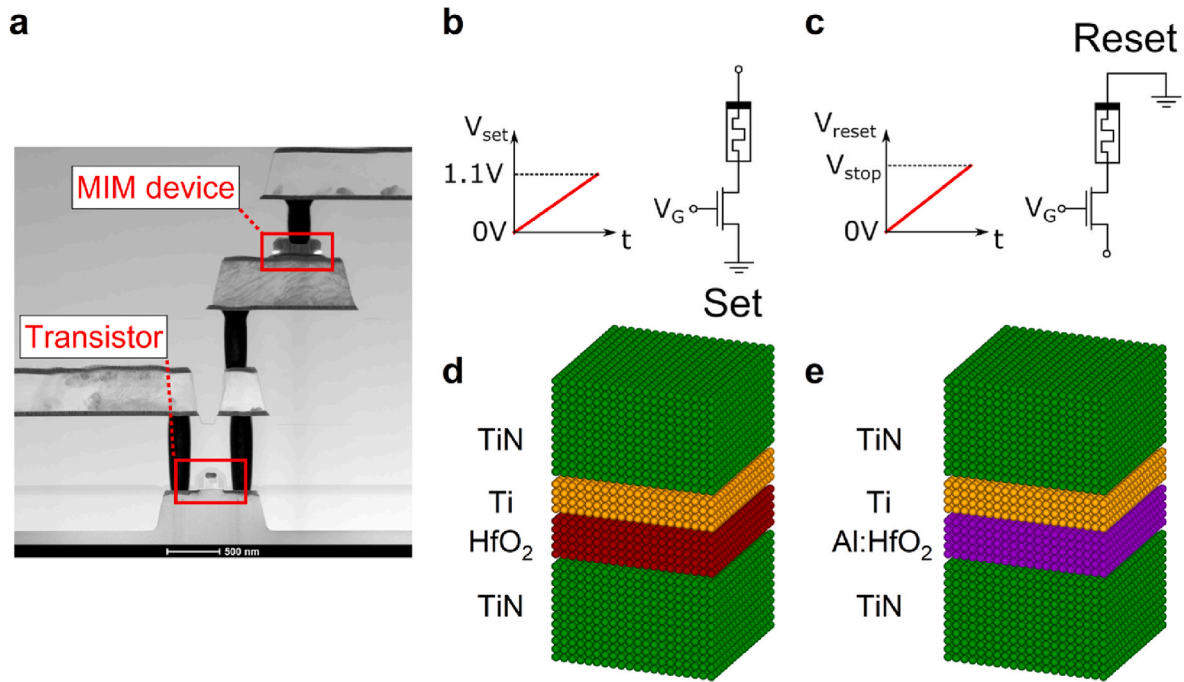
Fig. 1. a Cross-section transmission electron microscope (TEM) image of the 1T1R structure tested, schematics of the measurements describing **b** the set process, and **c** how V_{stop} is considered. Layer stack scheme of the **d** TiN/Ti/HfO$_2$/TiN and **e** TiN/Ti/Al:HfO$_2$/TiN devices.

processes) and the influence of the compliance current (I$_{cc}$) on the device switching and on charge conduction. By varying these parameters, we shed light on the influence of the RS processes on C2C variability.

In order to complement our experimental findings and offer a theoretical framework for interpretation, we turned to advanced simulations. Various simulation and modeling methodologies can be employed to address the intricacies of C2C and D2D variability, as well as the dynamics associated with switching phenomena. Current literature highlights various approaches to address these challenges. These approaches encompass compact modeling tailored for circuit simulation and design, kinetic Monte Carlo (kMC) [19–21] simulations and advanced statistical modeling [12,14,22]. In addition, an alternative yet complementary strategy involves the simulation of RRAM using circuit breakers (CB) [17,23]. CB-based simulation is positioned as an

intermediary numerical technique between kMC and compact modeling in terms of complexity and computing time. Nonetheless, it provides an acceptable description of RS processes and variability. Because of this, we have made use of a CB-based 3D simulator to describe our device operation. By employing advanced simulation methodologies, we provide a comprehensive understanding of the RS mechanisms in our devices. Our simulation approach shows the importance of integrating experimental analysis with advanced techniques to address the challenges in describing RS processes in memristive devices.

In the manuscript organization, section 2 provides detailed insights into the fabrication and measurement processes, section 3 unfolds the variability analysis and the modeling aspect. Finally, the main conclusions are drawn in section 4.
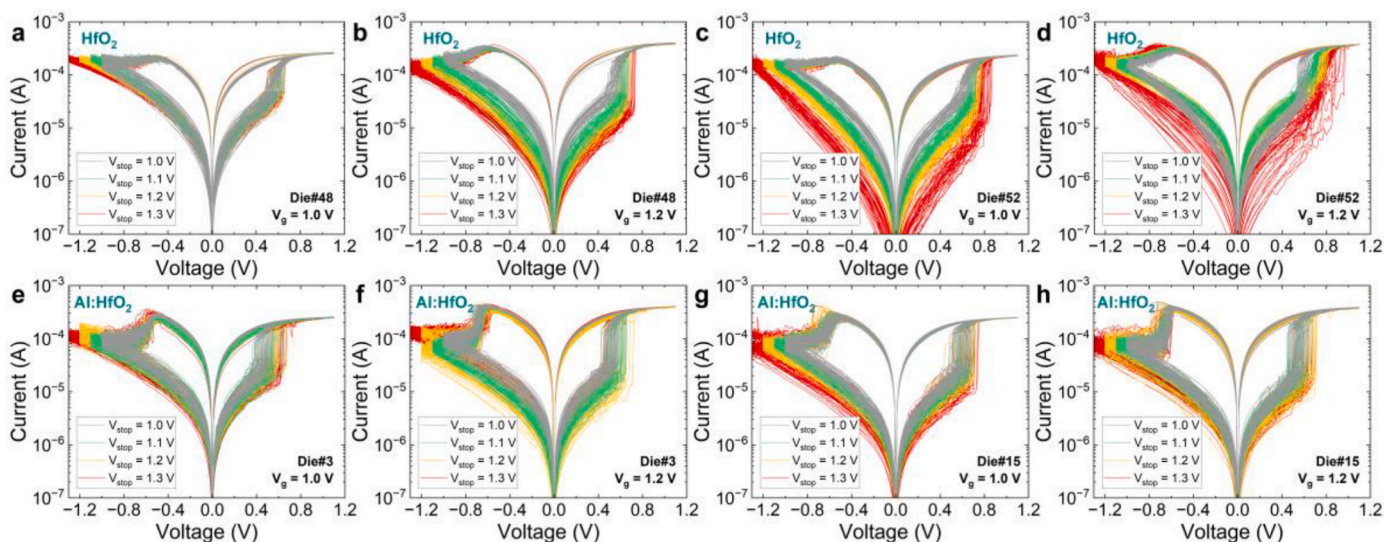
Fig. 2. I–V curves of set and reset cycles corresponding to **a**, **b**, **c**, **d** TiN/Ti/HfO$_2$/TiN devices, **e**, **f**, **g**, **h** TiN/Ti/Al:HfO$_2$/TiN devices for all the employed values of V_{stop} and V_G.
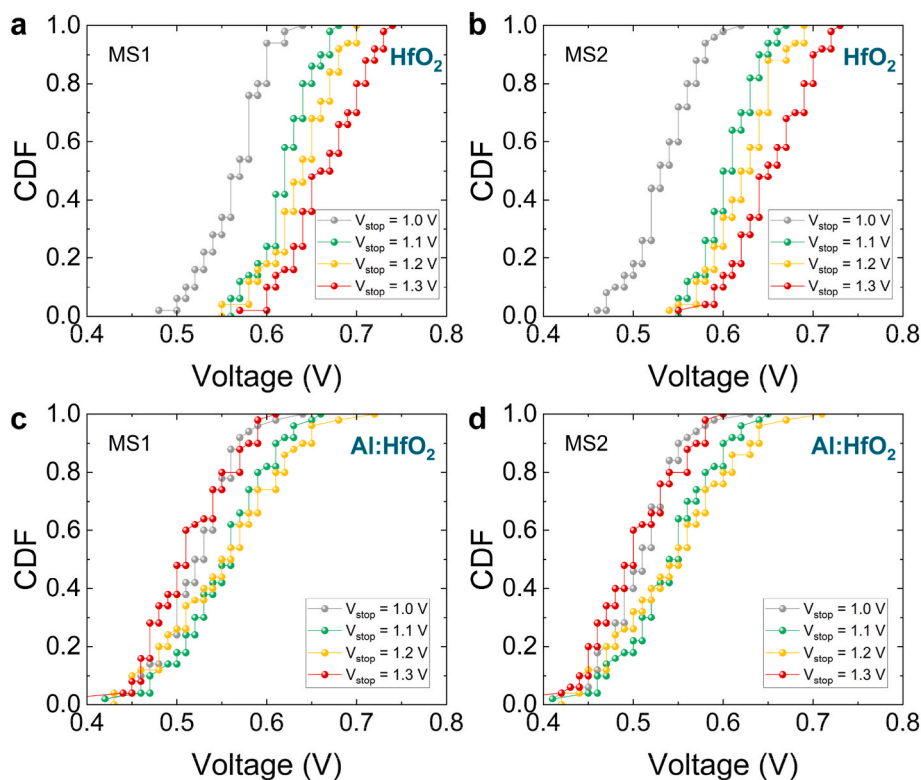
Fig. 3. CDFs of V_{set} for MS1 (MS2), **a** (**b**) for die #48 with $V_G = 1.2$ V corresponding to TiN/Ti/HfO$_2$/TiN devices, **c** (**d**) die #3 with $V_G = 1.2$ V corresponding to TiN/Ti/Al:HfO$_2$/TiN devices.

2. -Device fabrication and measurement

The devices were fabricated in a 130-nm CMOS process. Each memristive device is a 1-transistor-1-resistor (1T1R) structure consisting of a MIM stack connected in series to a select transistor, as shown in Fig. 1a. The MIM devices consist of a TiN/Ti/HfO$_2$/TiN stack (see Fig. 1d) and a TiN/Ti/Al:HfO$_2$/TiN stack (see Fig. 1e) with an area of 600×600 nm^2 placed on the metal line 2 of the CMOS process. The bottom electrode (BE) for both technologies is made of a 150 nm thick TiN layer, deposited by magnetron sputtering. Then, a 5 nm thick pure HfO$_2$ layer or a 4 nm HfO$_2$ layer with a doping of 5 % Al are respectively deposited by atomic layer deposition (ALD) (Fig. 1d–e respectively). Finally, the top electrodes (TE) are made of a 7 nm layer of Ti, acting as an oxygen scavenging layer and a 150 nm thick TiN layer, both deposited by magnetron sputtering.

Throughout the measurements, voltage sweeps were systematically applied to either the TE or to the source terminal of the transistor during the set and reset operations, respectively, while the other terminal was grounded. Voltage sweeps during the set operations ranged from 0.0 to 1.1 V with increments of 0.01 V, forcing an I_{CC} via the transistor gate terminal (V_G) with values 1.0 and 1.2 V. Thus, the corresponding I_{CC} for these V_G were estimated based on the characteristics of the transistor. For $V_G = 1.0$ V, I_{cc} was 250 μA and for $V_G = 1.2$ V, I_{cc} increased to 400 μA. For the reset operations, the voltage sweeps were applied from 0.0 V with a step of 0.01 V until reaching a V_{stop} (which refers to the maximum voltage applied during the reset operation of the memristive device) equal to the following values: 1.0, 1.1, 1.2 and 1.3 V for both V_G cases, see Fig. S1 in the Supplementary Information for a graphical depiction of the whole experiment.

We performed a forming process prior to the operation of the devices. Then, we measured several groups of 50 reset-set I–V curves under the ramped voltage stress (RVS) operating regime, in each of the devices considered. Four distinct dies, namely Die#3 and Die#15 corresponding to the TiN/Ti/HfO$_2$/TiN stack and Die#48 and Die#52 for the TiN/Ti/

Al:HfO$_2$/TiN stack were measured. For each group of 50 I–V curves a different stop voltage was employed during the reset process. Die#3 and Die#48 underwent measurements within a V_{stop} range from 1.0 V to 1.3 V, while Dies#15 and Die#52 were measured in the reverse direction, ranging from 1.3 V to 1.0 V. This approach was adopted to account for the impact of both increasing and decreasing V_{stop} on the experimental outcomes also considering a different current level. These measurements were performed for both V_G values mentioned before, namely, 1.0 and 1.2 V. See Fig. 2 for the I–V representation of all the measurements and Fig. S2 for the comparison of the calculated mean current values for both technologies.

The extraction of RS parameters (reset and set voltages and currents) is performed with advanced numerical techniques, see Fig. S3. For the set, Method Set 1 (MS1) is based on the localization of the maximum value of the current derivative [18]; Method Set 2 (MS2) searches for the set I–V curve knee [18]. In what is related to the reset voltage we used different extraction techniques, see Fig. S3b for further information. Method Reset 1 (MR4 in Ref. [18]) is based on the localization of the first point with decreasing current, and Method Reset 2 (MR5 in Ref. [18]) is obtained by performing the charge derivative with respect to the flux and detecting when this derivative is null.

3. Results and discussion

3.1. Preliminary analysis

The cumulative distribution functions (CDFs) for the set voltages (V_{set}) are shown in Fig. 3 for Die#48 and Die#3 both measured with $V_G = 1.2$ V. The corresponding currents (I_{set}) for these particular dies are presented in Fig. S4.

See that the lower the V_{stop} is, the weaker is the corresponding reset process and, therefore, the lower is the voltage needed for the conductive filament (CF) formation in the following set process. In general, the set voltage values for both MS1 and MS2 methodologies are higher for
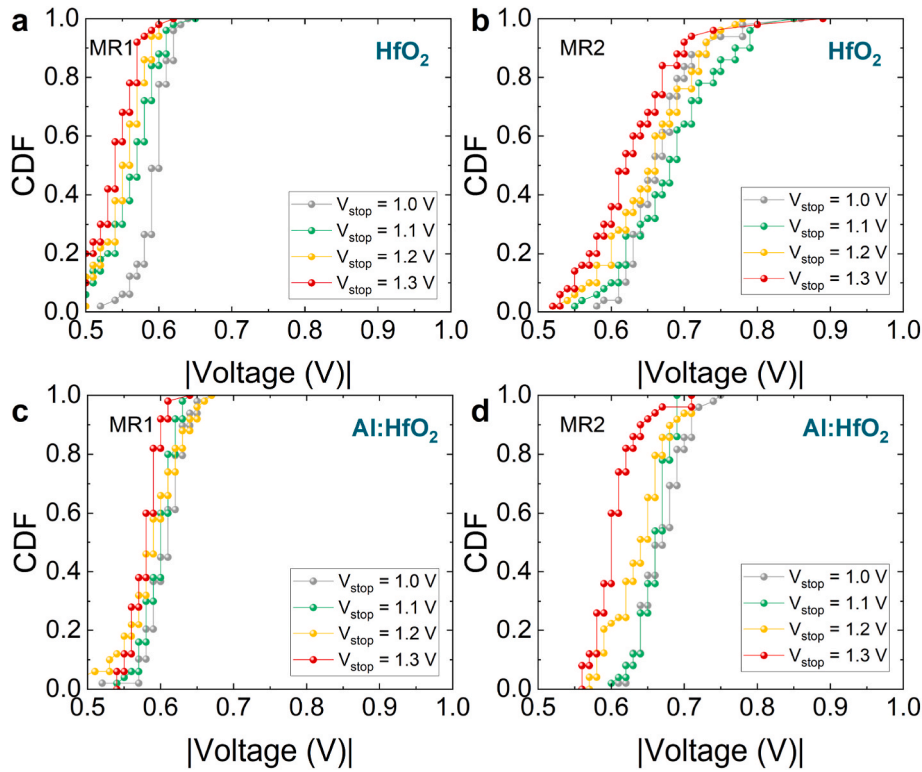
Fig. 4. CDFs of V_{reset} for MR1 (MR2), **a**, (**b**) for die #48 with $V_G = 1.2$ V corresponding to TiN/Ti/HfO$_2$/TiN devices, **c** (**d**) for die #3 with $V_G = 1.2$ V corresponding to TiN/Ti/Al:HfO$_2$/TiN devices.

the TiN/Ti/HfO$_2$/TiN devices than for the TiN/Ti/Al:HfO$_2$/TiN, denoting the positive effects of Al doping for the RS. The results are affected by the inherent variability of these devices [12,14,15]. Regarding the set current, for MS1, no clear trend emerges due to cycle-to-cycle variability and the numerical particularities of the extraction method. Conversely, MS2 exhibits an inverse relationship for some stop voltages: higher values of V_{stop} result in lower current values. This phenomenon arises because, as previously mentioned, a stronger CF rupture leads to lower current values. Note also that, again, higher current values are seen for TiN/Ti/HfO$_2$/TiN devices.

The CDFs for the reset voltages corresponding to Fig. 3 are shown in Fig. 4.

In general, it can be seen the opposite trend highlighted above. The

lower the stop voltage, the higher the reset voltage because the CF is stronger (the density of oxygen vacancies is higher [19,20]) and, therefore, it is harder to break. Regarding the corresponding current values, a similar tendency can be observed as for the reset voltages, as depicted in Fig. S5. These results reinforce the statement that variations in V_{stop} directly influence the CF density and, consequently, the current flowing through the device during the reset process. Thus, higher V_{stop} values correspond to weaker and more resistive CFs.

The rest of the analyzed devices presented in Fig. 2 can be found in the Supplementary Information. In particular, regarding the set cycles, the CDFs for V_{set} (I_{set}) are shown in Fig. S6 (S7) for Die#48 and Die#3, both measured with $V_G = 1.0$ V. Additionally, the CDFs for V_{set} (I_{set}) are shown in Fig. S8 (S9) for Die#52 and Die#15, both measured with $V_G =$
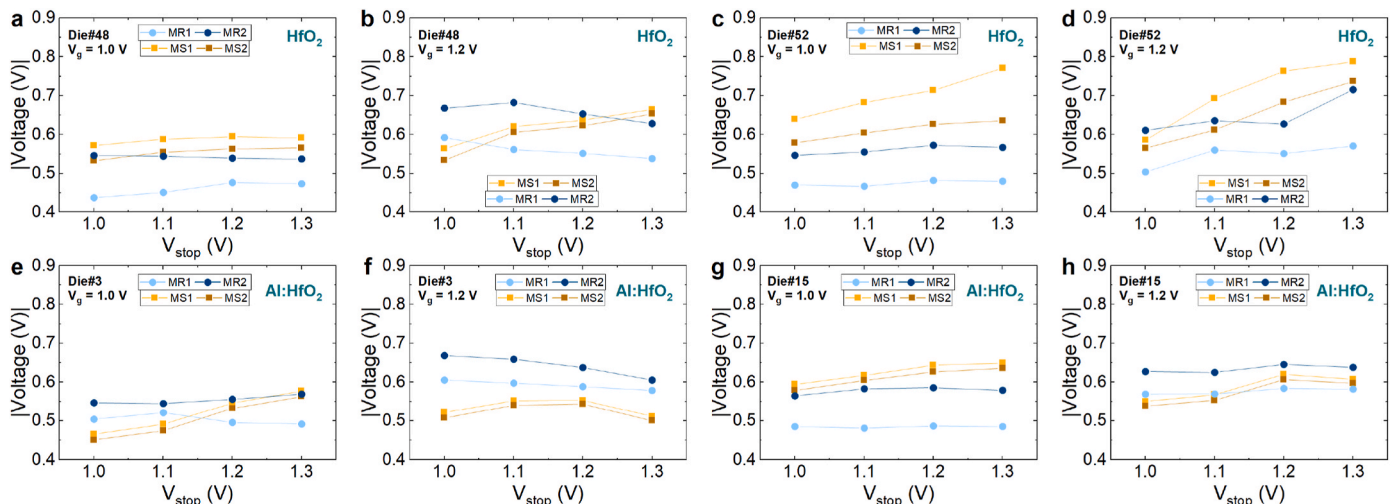
Fig. 5. V_{set} (V_{reset}) mean extracted with MS1 and MS2 (MR1, MR2) [18] versus V_{stop} for **a**, **b**, **c**, **d** TiN/Ti/HfO$_2$/TiN devices, **e**, **f**, **g**, **h** TiN/Ti/Al:HfO$_2$/TiN devices.
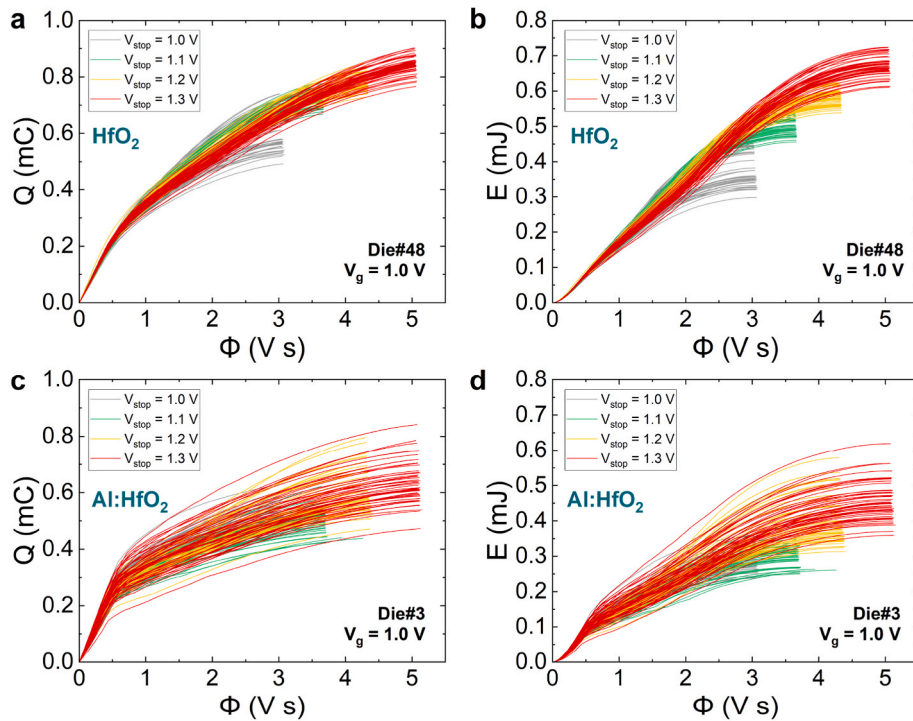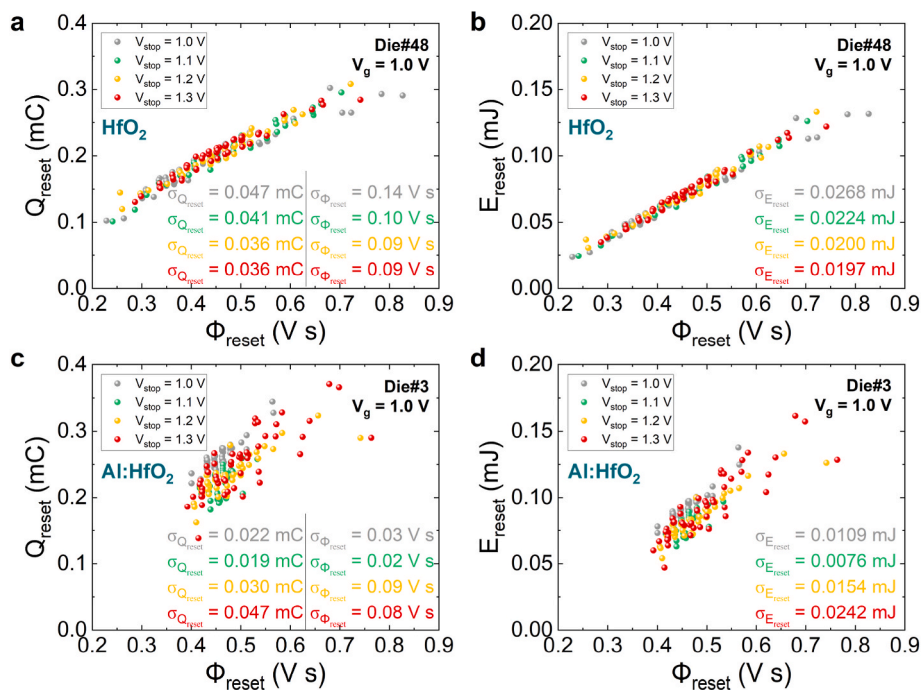
Fig. 6. **a (c)** Charge versus flux data for Die#48 (Die#3) with $V_G = 1.0$ V corresponding to TiN/Ti/HfO$_2$/TiN (TiN/Ti/Al:HfO$_2$/TiN) devices, **b (d)** energy versus flux data for Die#48 (Die#3) with $V_G = 1.0$ V corresponding to TiN/Ti/HfO$_2$/TiN (TiN/Ti/Al:HfO$_2$/TiN) devices.

1.0 V. Furthermore, CDFs for V_{set} (I_{set}) are shown in Fig. S10 (S11) for Die#52 and Die#15, both measured with $V_G = 1.2$ V. These results follow the tendencies explained above, indicating that the set voltages and currents exhibit predictable and consistent behavior across different devices and technologies. However, for the reset cycles, there are no general trends in the reset voltages and currents. This lack of consistent patterns for the reset parameters can be attributed to the fact that after the V_{stop} application, the set event occurs, the filament is broken, and the

effects of C2C variability are more significative in the reset events, masking the V_{stop} role.

In Fig. 5, the mean values for V_{set} and V_{reset}, extracted using previously detailed methods, are presented for all the experimental data following the sequence of Fig. 2. Despite variability, a notable correlation between the mean values of V_{set} and V_{stop} is evident for various die configurations. Specifically, as V_{stop} increases, there is a corresponding increase in V_{set}, a trend particularly pronounced in HfO$_2$ devices

Fig. 7. **a (c)** Extracted charge and flux data at the reset point for Die#48 (Die#3) with $V_G = 1.0$ V corresponding to TiN/Ti/HfO$_2$/TiN (TiN/Ti/Al:HfO$_2$/TiN) devices, **b (d)** extracted energy and flux data at the reset point for Die#48 (Die#3) with $V_G = 1.0$ V corresponding to TiN/Ti/HfO$_2$/TiN (TiN/Ti/Al:HfO$_2$/TiN) devices.
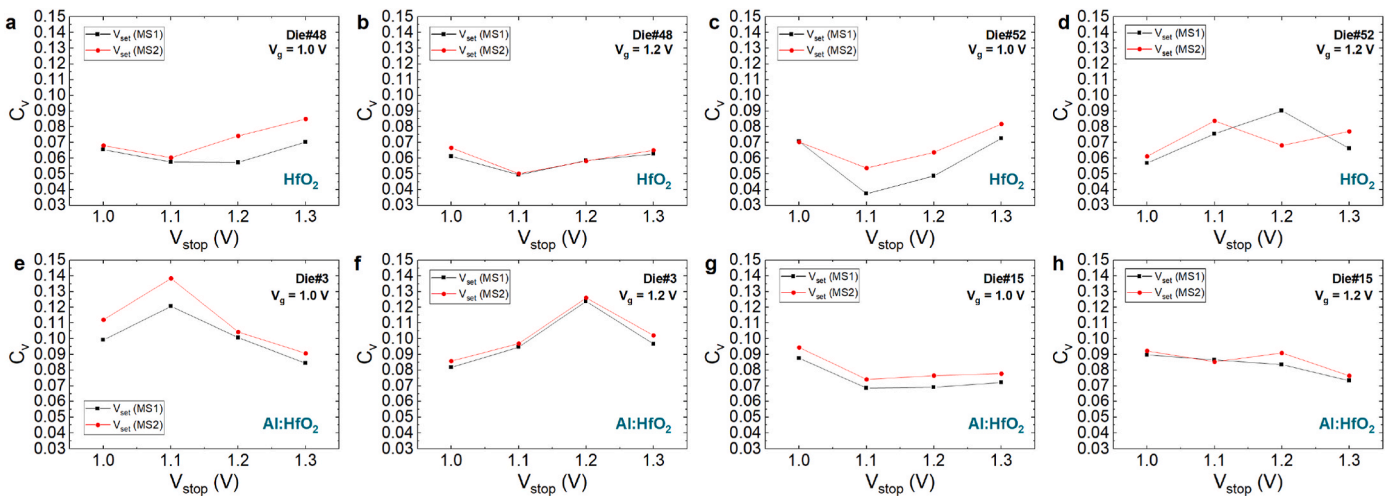
Fig. 8. V_{set} coefficient of variation extracted with MS1 and MS2 [18] versus V_{stop} for **a, b, c, d** TiN/Ti/HfO$_2$/TiN devices, **e, f, g, h** TiN/Ti/Al:HfO$_2$/TiN devices.

compared to their Al:HfO$_2$ counterparts. Conversely, discernible trends are absent for V_{reset} values; however, it is worth noting that these parameters exhibit a notable increase for $V_g = 1.2$ V compared to $V_g = 1.0$ V in both technologies. The corresponding mean values for the current are presented in Fig. S12.

3.2. -Variability analysis

When studying the variability linked to the switching process, it is interesting to consider the injected charge (see Equation (1)), as well as the flux (see Equation (2)) during the reset operation.

$$Q(t) = \int_0^t i(t') \, dt' \tag{1}$$

$$\Phi(t) = \int_0^t v(t') \, dt' \tag{2}$$

$$E(t) = \int_0^t i(t') \, v(t') \, dt' \tag{3}$$

As the integrals are considered in a complete cycle, overall variations can be observed. We have determined these magnitudes and plotted them together in Fig. 6 for a particular die for both technologies. The distributions of the injected charge until the reset event are obtained,

Q_{reset}, versus the corresponding flux, ϕ_{reset} (Fig. 7a–c corresponding to HfO$_2$ and Al:HfO$_2$ respectively), are shown for the four different stop voltages considered. A strong correlation can be seen between the variables, as expected due to the intrinsic relationship between charge and flux in the context of RS phenomena in memristors (it is clearer in the HfO$_2$ dielectric case). The flux, being the integral of the applied voltage over time, directly influences the electric field driving ion or vacancy movement. Hence, a higher flux implies a stronger or more prolonged electric field, resulting in a greater degree of charge injection, needed to induce the reset event.

In addition, we obtained the energy delivered to the device till the CF is disrupted (see Equation (3)). In Fig. 7b–d, the energy till the reset event is plotted, E_{reset} versus ϕ_{reset}. The Standard Deviation (SD) for these magnitudes has been calculated for all the V_{stop} values, revealing correlation in some cases (inset in the panels of Fig. 7). For the Al:HfO$_2$ devices, this parameter is generally lower, indicating reduced variability across different V_{stop} values. Furthermore, it should be noted that for higher fluxes, the point cloud spreads due to cycle-to-cycle variability. The results corresponding to $V_G = 1.2$ V are shown in Fig. S13.

In addition, the mean values of Φ_{reset}, Q_{reset}, t_{reset}, and E_{reset} are shown in Fig. S14 for all the dies measured corresponding to both technologies. Notably, there is an average increase in all these parameters as V_{stop} increases for Die#52 and $V_G = 1.2$ V in the case of HfO$_2$ devices. It is remarkable for this measurement conditions that,
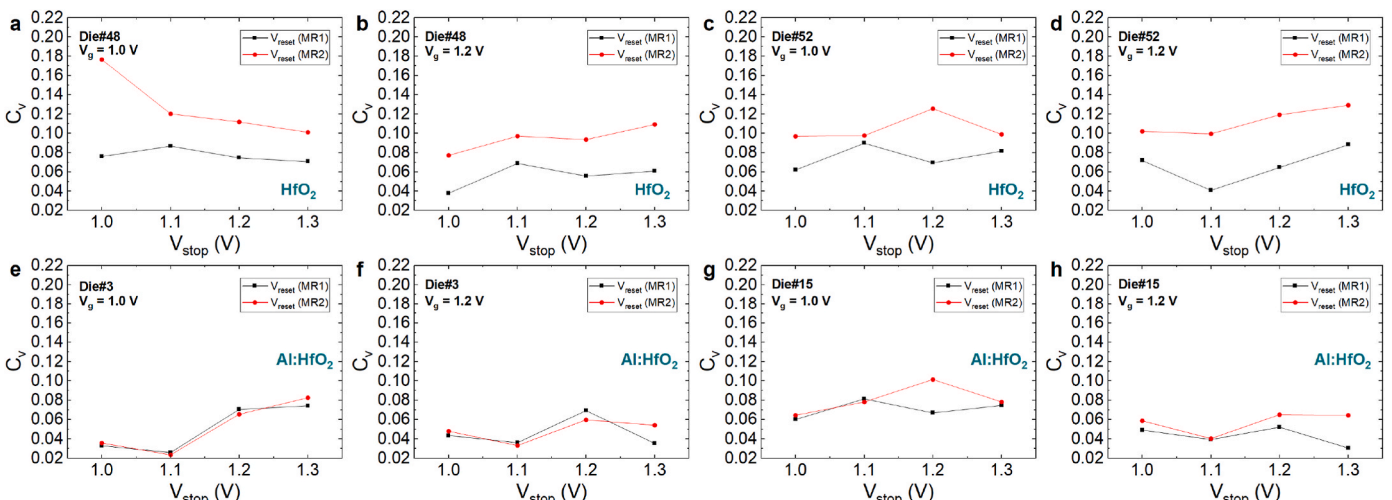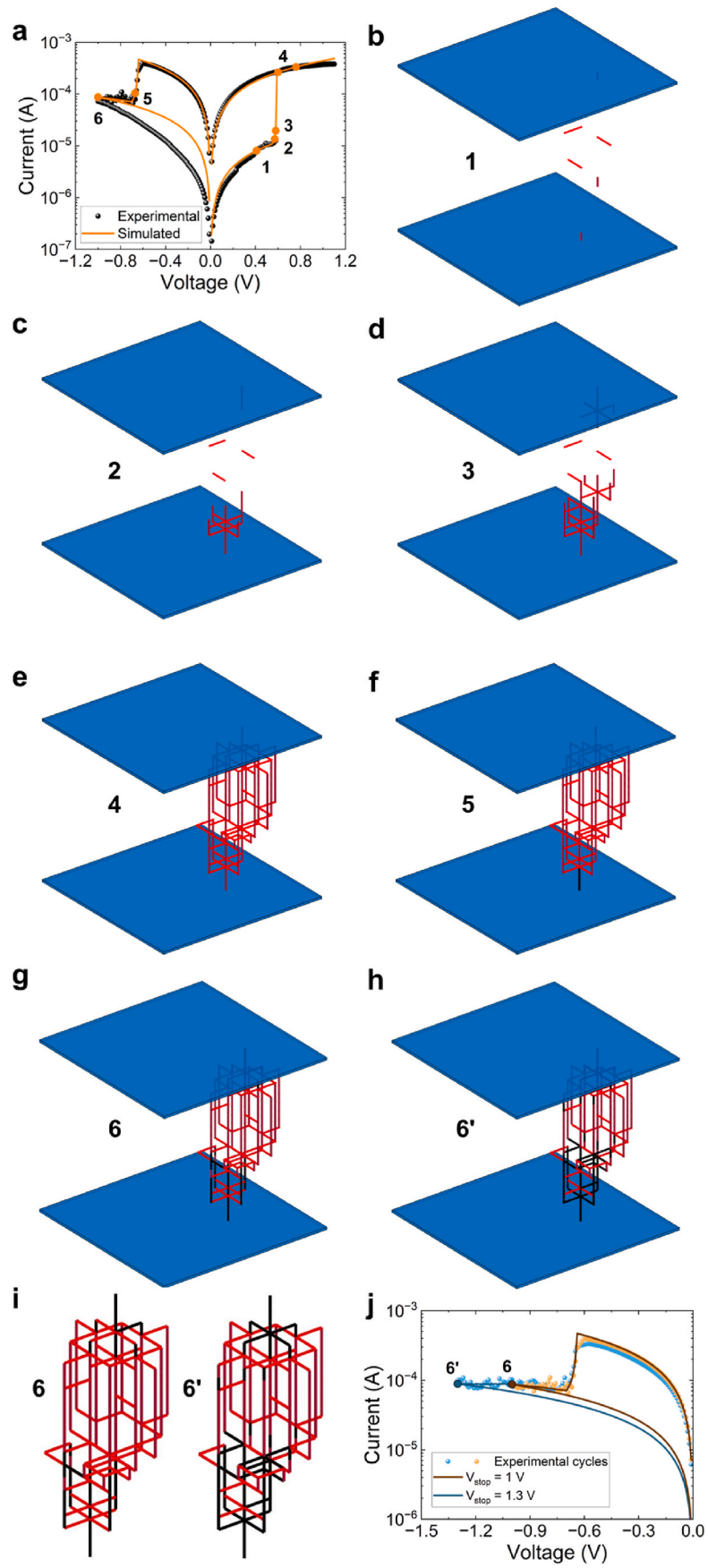

Fig. 9. V_{reset} coefficient of variation extracted with MR1 and MR2 [18] versus V_{stop} for **a, b, c, d** TiN/Ti/HfO$_2$/TiN devices, **e, f, g, h** TiN/Ti/Al:HfO$_2$/TiN devices.

Fig. 10. a Simulated (orange line) and experimental (black symbols) current versus voltage in a set and reset process. See different points along the I–V that correspond to different CNF formation and rupture stages (the CNFs are plotted in panels **b–g**). A $20 \times 10 \times 10$ network was employed to obtain this simulation using CBs with three resistance levels: $R_{off2} = 2.6 \times 10^5 \, \Omega$, $R_{off} = 2.5 \times 10^3 \, \Omega$, $R_{on} = 170 \, \Omega$. The model parameters are: $V_{off} = 0.1$ V, $V_{off2} = 0.2$ V, $V_{on} = 0.046$ V, $V_{on2} = 0.065$ V, **h** CF rupture corresponding to a simulated curve for a reset process using a $V_{stop} = 1.3$ V for the point highlighted in Fig. 10j, **i** CF comparison for the simulated curves depicted in Fig. 10j **j** Simulated current versus voltage for a reset process using a $V_{stop} = 1$ V (orange line) and $V_{stop} = 1.3$ V (blue line). The simulation parameters are the same as in Fig. 10a.

independently of the technology, a drop in all the parameters is observed at $V_{stop} = 1.1$ V. Conversely, for Die#48 and $V_G = 1.2$ V (measured in the opposite order, that is, V_{stop} from 1.0 to 1.3 V), the trend is the opposite; as V_{stop} rises, the mean values of all parameters decrease. This contrasting behavior suggests a gradual decrease in mean values as the measurement progresses. Therefore, accounting for these previous results, V_{stop} is essential to fix the device operating point, and therefore, to shorten the switching times and reduce the device energy consumption when operating them in a digital context as non-volatile memories.

The coefficient of variation (Cv, standard deviation/mean of the distribution of values obtained) has been previously employed [24] to quantify cycle-to-cycle variability in these devices. In Fig. 8 the values of the coefficient of variation for V_{set} versus V_{stop} are shown for each measured die. Notably, dies corresponding to the HfO$_2$ device exhibit a slight increase in the Cv as V_{stop} rises for both values of V_G (considering the variability is inherent to the RS). Conversely, dies for Al:HfO$_2$ do not display a clear trend. This situation is also observed for the reset voltages (Fig. 9). For HfO$_2$ devices, Cv values are generally higher than for the Al: HfO$_2$ case, showing also a higher variability. For the case of the set (reset) currents, in Fig. S15 (S16), the trends are not so obvious as the cycle-to-cycle variability blurs any clear behaviour.

The Cv has also been obtained for the flux, the injected charge, the time to reset and energy needed to switch the device, see Fig. S17 in the Supplementary Information. The results reveal again the overall Cv dependence on V_{stop} although variability [14] masks clear trends in the results.

3.3. -Modeling and simulation

We have made use of a 3D simulation tool based on CBs to analyze the resistance switching and charge conduction in our devices. This tool enables the dynamic description of CFs; in particular, the creation and destruction processes that lead to RS, providing a comprehensive representation of both unipolar and bipolar device operations [23]. We performed simulations on the devices outlined in Section II using a $20 \times 10 \times 10$ matrix of resistors to account for the 5 nm-thick dielectric layer. By modeling the device in three dimensions, we can accurately capture the spatial distribution of electric fields and current paths within the dielectric layer; by doing so, the dynamics of CF rupture and formation processes is capture since they are purely 3D. The CF evolution is described as a function of the applied voltage and time; the information obtained help on the analysis of the device variability. We have used 20 CB layers in order to account for a CB in a grid size of 0.25 nm, which is in line with other techniques such as kinetic Monte Carlo simulation tools [19–21,25].

A three-value CB resistance model was employed, see Fig. S18. The simulation parameters are selected by means of a tuning process using experimental I–V characteristics, ensuring that the modeled behavior closely matches the measured RS behavior in actual devices. Fig. 10a displays the fitting of an experimental I–V curve, with different points marked along the curve to trace the CF evolution. In Fig. 10b–h, low resistance value CBs (R_{on}) are depicted in red and high resistance value CBs (R_{off}) in black. The second value of the high resistance CBs (R_{off2}) corresponds to the majority of the grid but this resistance is omitted here for the sake of clarity. The progression of the set process illustrates the formation of the CF, Fig. 10b–d. In Fig. 10e, the CF short-circuits the electrodes, forming a fully-established conduction path. The subsequent points (f-g) represent the reset process, where the filament is partially

broken. See in Fig. 10h the status of the CNF when instead of employing a V_{stop} of 1.0 V, a 1.3 V value is assumed. The comparison of the CFs remnants for the V_{stop} values employed is shown in Fig. 10i. See how the CF for the higher V_{stop} has less CBs with low resistance values included (red lines); this means that it is more resistive and the CF compacity is lower, as expected. This explains the higher set voltages shown in Fig. 3 at higher stop voltages, since a higher voltage is needed to reform an already weaker CF. In Fig. 10j, the same simulation corresponding to Fig. 10a, for two different V_{stop} values (1.0 V and 1.3 V), is shown.

4. Conclusions

This study comprehensively analyzes the RS behavior in 1T1R HfO$_2$-based memristors, addressing both C2C and D2D variability. We describe the manner V_{stop} and V_G impact RS parameters and observe that higher V_{stop} values lead to device stronger CF ruptures that highlight the importance of optimizing V_{stop} to achieve a reliable switching. V_G influences the current flowing through the RS device, which in turn affects the RS behavior. Our experiments showed that a V_G of 1.2 V leads to higher currents, consequently enhancing the RS process and reducing variability. Various numerical methods for extracting RS parameters were compared. The TiN/Ti/Al:HfO$_2$/TiN devices demonstrated improved performance over TiN/Ti/HfO$_2$/TiN devices, with enhanced stability and endurance as a consequence of aluminum doping, that improves RS features. In addition, advanced simulation methodologies, including circuit breaker-based 3D simulations, provided detailed models of RS phenomena. The study confirms the critical role of D2D and C2C variability in device performance, emphasizing the need for precise control of operating conditions to enhance reliability. These findings contribute to developing and improving robust parameter extraction methodologies, which are essential for the industrial application of HfO$_2$-based memristors.

CRediT authorship contribution statement

David Maldonado: Writing – review & editing, Writing – original draft, Software, Data curation, Conceptualization. **Antonio Cantudo:** Software. **Keerthi Dorai Swamy Reddy:** Investigation. **Stefan Pechmann:** Data curation, Conceptualization. **Max Uhlmann:** Investigation. **Christian Wenger:** Writing – review & editing, Resources, Project administration. **Juan Bautista Roldan:** Writing – review & editing, Writing – original draft, Software. **Eduardo Perez:** Writing – review & editing, Writing – original draft, Supervision, Project administration, Conceptualization.

Declaration of competing interest

Data availability

Data will be made available on request.

Acknowledgements

Appendix A. Supplementary data

Supplementary data to this article can be found online at https://doi.org/10.1016/j.mssp.2024.108726.

References

[1] M. Lanza, A. Sebastian, W.D. Lu, M.L. Gallo, M. Chang, D. Akinwande, F.M. Puglisi, H.N. Alshareef, M. Liu, J.B. Roldan, Memristive technologies for data storage, computation, encryption, and radio-frequency communication, Science 376 (6597) (2022), https://doi.org/10.1126/science.abj9979.

[2] J. Tang, F. Yuan, X. Shen, Z. Wang, M. Rao, Y. He, Y. Sun, X. Li, W. Zhang, Y. Li, B. Gao, H. Qian, G. Bi, S. Song, J.J. Yang, H. Wu, Bridging biological and artificial neural networks with emerging neuromorphic devices: fundamentals, progress, and challenges, Adv. Mater. 31 (49) (2019), https://doi.org/10.1002/adma.201902761.

[3] R. Romero-Zaliz, A. Cantudo, E. Perez, F. Jimenez-Molinos, C. Wenger, J.B. Roldan, An analysis on the architecture and the size of quantized hardware neural networks based on Memristors, Electronics 10 (24) (2021) 3141, https://doi.org/10.3390/electronics10243141.

[4] M.A. Khan, S. Yim, S. Rehman, F. Ghafoor, H. Kim, H. Patil, M.F. Khan, J. Eom, Two-dimensional materials memory devices with floating metal gate for neuromorphic applications, Materials Today Advances 20 (2023) 100438, https://doi.org/10.1016/j.mtadv.2023.100438.

[5] K.A. Rokade, D.D. Kumbhar, S.L. Patil, S.S. Sutar, K.V. More, P.B. Dandge, R. K. Kamat, T.D. Dongale, CogniFiber: harnessing biocompatible and biodegradable 1D collagen nanofibers for sustainable nonvolatile memory and synaptic learning applications, Adv. Mater. (2024), https://doi.org/10.1002/adma.202312484.

[6] E.P. Quesada, R. Romero-Zaliz, E. Pérez, M.K. Mahadevaiah, J. Reuben, M. A. Schubert, J. Jiménez-Molinos, J.B. Roldán, C. Wenger, Toward reliable compact modeling of multilevel 1T-1R RRAM devices for neuromorphic systems, Electronics 10 (6) (2021) 645, https://doi.org/10.3390/electronics10060645.

[7] Memristive Devices for Brain-Inspired Computing, Elsevier eBooks, 2020, https://doi.org/10.1016/c2017-0-04786-9.

[8] j.S. Lee, S. Lee, T.W. Noh, Resistive switching phenomena: a review of statistical physics approaches, Appl. Phys. Rev. 2 (3) (2015), https://doi.org/10.1063/1.4929512.

[9] H.P. Wong, H. Lee, S. Yu, Y. Chen, Y. Wu, P. Chen, B. Lee, F.T. Chen, M. Tsai, Metal–oxide RRAM, Proc. IEEE 100 (6) (2012) 1951–1970, https://doi.org/10.1109/jproc.2012.2190369.

[10] S. Yu, Semiconductor memory devices and circuits. https://doi.org/10.1201/9781003138747, 2022.

[11] M. Lanza, H.P. Wong, E. Pop, D. Ielmini, D. Strukov, B.C. Regan, L. Larcher, M. A. Villena, J.J. Yang, L. Goux, A. Belmonte, Y. Yang, F.M. Puglisi, J. Kang, B. Magyari-Köpe, E. Yalon, A. Kenyon, M. Buckwell, A. Mehonic, Y. Shi, Recommended methods to study resistive switching devices, Advanced Electronic Materials 5 (1) (2018), https://doi.org/10.1002/aelm.201800143.

[12] E. Pérez, D. Maldonado, C. Acal, J. Ruiz-Castro, F. Alonso, A. Aguilera, F. Jiménez-Molinos, C. Wenger, J. Roldán, Analysis of the statistics of device-to-device and cycle-to-cycle variability in TiN/Ti/Al:HfO2/TiN RRAMs, Microelectron. Eng. 214 (2019) 104–109, https://doi.org/10.1016/j.mee.2019.05.004.

[13] A. Chen, M. Lin, Variability of resistive switching memories and its impact on crossbar array performance. 2011 International Reliability Physics Symposium, IEEE Xplore, 2011, pp. MY.7.1–MY.7.4, https://doi.org/10.1109/irps.2011.5784590.

[14] J.B. Roldán, E. Miranda, D. Maldonado, A.N. Mikhaylov, N.V. Agudov, A. A. Dubkov, M.N. Koryazhkina, M.B. González, M.A. Villena, S. Poblador, M. Saludes-Tapia, R. Picos, F. Jiménez-Molinos, S.G. Stavrinides, E. Salvador, F. J. Alonso, F. Campabadal, B. Spagnolo, M. Lanza, L.O. Chua, Variability in resistive memories, Advanced Intelligent Systems 5 (6) (2023), https://doi.org/10.1002/aisy.202200338.

[15] E. Perez, D. Maldonado, E.P. Quesada, M.K. Mahadevaiah, F. Jimenez-Molinos, C. Wenger, J.B. Roldan, Parameter extraction methods for assessing Device-to-Device and Cycle-to-Cycle variability of memristive devices at WAFER Scale. I.E.E. E. Transactions on Electron Devices, IEEE Trans. Electron. Dev. 70 (1) (2023) 360–365, https://doi.org/10.1109/ted.2022.3224886.

[16] D.D. Kumbhar, S. Kumar, M. Dubey, A. Kumar, T.D. Dongale, S.D. Pawar, S. Mukherjee, Exploring statistical approaches for accessing the reliability of Y2O3-based memristive devices, Microelectron. Eng. 288 (2024) 112166, https://doi.org/10.1016/j.mee.2024.112166.

[17] D. Maldonado, S. Aldana, M. González, F. Jiménez-Molinos, M. Ibáñez, D. Barrera, F. Campabadal, J. Roldán, Variability estimation in resistive switching devices, a numerical and kinetic Monte Carlo perspective, Microelectron. Eng. 257 (2022) 111736, https://doi.org/10.1016/j.mee.2022.111736.

[18] D. Maldonado, S. Aldana, M. González, F. Jiménez-Molinos, F. Campabadal, J. Roldán, Parameter extraction techniques for the analysis and modeling of resistive memories, Microelectron. Eng. 265 (2022) 111876, https://doi.org/10.1016/j.mee.2022.111876.

[19] S. Aldana, P. García-Fernández, R. Romero-Zaliz, M.B. González, F. Jiménez-Molinos, F. Gómez-Campos, F. Campabadal, J.B. Roldán, Resistive switching in HfO2 based valence change memories, a comprehensive 3D kinetic Monte Carlo approach, Journal of Physics. D, Applied Physics 53 (22) (2020) 225106, https://doi.org/10.1088/1361-6463/ab7bb6.

[20] S. Aldana, E. Pérez, F. Jiménez-Molinos, C. Wenger, J.B. Roldán, Kinetic Monte Carlo analysis of data retention in Al:HfO2-based resistive random access memories, Semicond. Sci. Technol. 35 (11) (2020) 115012, https://doi.org/10.1088/1361-6641/abb072.

[21] S. Dirkmann, J. Kaiser, C. Wenger, T. Mussenbrock, Filament growth and resistive switching in hafnium oxide memristive devices, ACS Appl. Mater. Interfaces 10 (17) (2018) 14857–14868, https://doi.org/10.1021/acsami.7b19836.

[22] J.B. Roldán, F.J. Alonso, A.M. Aguilera, D. Maldonado, M. Lanza, Time series statistical analysis: a powerful tool to evaluate the variability of resistive switching memories, J. Appl. Phys. 125 (17) (2019), https://doi.org/10.1063/1.5079409.

[23] D. Maldonado, A. Cantudo, F.M. Gómez-Campos, Y. Yuan, Y. Shen, W. Zheng, M. Lanza, J.B. Roldán, 3D simulation of conductive nanofilaments in multilayer h-BN memristors via a circuit breaker approach, Mater. Horiz. 11 (4) (2024) 949–957, https://doi.org/10.1039/d3mh01834b.

[24] H. Kim, M.R. Mahmoodi, H. Nili, D.B. Strukov, 4K-memristor analog-grade passive crossbar circuit, Nat. Commun. 12 (1) (2021), https://doi.org/10.1038/s41467-021-25455-0.

[25] S. Aldana, P. García-Fernández, A. Rodríguez-Fernández, R. Romero-Zaliz, M. B. González, F. Jiménez-Molinos, F. Campabadal, F. Gómez-Campos, J.B. Roldán, A 3D kinetic Monte Carlo simulation study of resistive switching processes in Ni/HfO2/Si-n+-based RRAMs, Journal of Physics. D, Applied Physics 50 (33) (2017) 335103, https://doi.org/10.1088/1361-6463/aa7939.